

Nanosecond-pulsed dielectric barrier discharge-based plasma-assisted anti-icing: modeling and mechanism analysis

Yifei Zhu^{1,2}, Yun Wu^{1,2}, Biao Wei², Haojun Xu², Hua Liang², Min Jia², Huimin Song² and Yinghong Li¹

¹ Institute of Aero-engine, School of Mechanical Engineering, Xi'an Jiaotong University, Xi'an 710049, People's Republic of China

² Science and Technology of Plasma Dynamics Laboratory, Xi'an 710038, People's Republic of China

E-mail: wuyun1223@126.com

Received 14 August 2019, revised 12 December 2019

Accepted for publication 23 December 2019

Published 23 January 2020



Abstract

The characteristics of nanosecond-pulsed dielectric barrier discharge (nSDBD) in an anti-icing configuration is studied. The mechanisms and energy characteristics of the nSDBD-based plasma-assisted anti-icing are analyzed using a numerical model and existing experimental data. Two-dimensional simulations based on PASSKEY (PARallel Streamer Solver with KinEtics) code are conducted. The code couples a self-consistent fluid model with detailed kinetics, an efficient photo-ionization model, Euler equations and a heat transfer equation for solid materials. The results of icing wind tunnel experiments conducted by two groups are analyzed together. The reduced electric field and the electron density are examined for high-voltage pulses with 800 ns and 20 ns width. The 'merge' of counter-propagating surface streamers with the same polarity is numerically observed under high-voltage amplitude. The effects of gas heating and solid heating in time scales of one pulse and one duty cycle are compared, and the key mechanism for icing prevention is direct fast gas-heating energy transfer from gas to ice/water accumulated on the surface in each duty cycle.

Keywords: nanosecond-pulsed surface dielectric barrier discharge, nSDBD, plasma anti-icing, plasma modeling

(Some figures may appear in colour only in the online journal)

1. Introduction

Surface dielectric barrier discharges (SDBDs) have been studied for decades in the aerodynamics community. A typical SDBD device consists of a high-voltage electrode placed above the dielectric surface, and a low-voltage (typically grounded or at constant potential) electrode placed below the dielectric surface [1–4]. At atmospheric pressure, microdischarges appear stochastically in the vicinity of the high-voltage electrode and develop into streamers propagating along the dielectric surface, generating ionic wind and gas flow. For typical ac voltage amplitudes from a few kV to 20–30 kV and frequencies in the range of 1–10 kHz,

acSDBDs can generate a flow of a few ms^{-1} (up to 10ms^{-1}). When the high-voltage pulses are shortened to tens or hundreds of nanoseconds, the streamers start synchronously from the high-voltage electrode and propagate along the dielectric. In the case of nanosecond-pulsed SDBD (nSDBD), the ionic wind is no longer observed; instead a micro perturbation wave will be generated from the edge of the electrode due to fast release of the energy stored in the electronically excited states [5–8]. The features of ionic wind generation and fast gas heating of SDBDs have been studied and utilized in applications such as plasma-assisted flow control [9–14] and plasma-assisted ignition/combustion by different groups since the early 2000s.

The energy from discharge will be released through gas/dielectric heating [15]. Comparing to a traditional heating strategy, e.g. resistance heating, SDBD-based heating has higher energy efficiency and faster rate of temperature increase, and thus has attracted the interest of anti-icing groups. Ice accretion could occur on almost all exposed frontal components when an aircraft is traveling through frozen clouds with super-cooled water droplets, changing the aerodynamic characters and weights of some critical components (i.e. airfoil, vertical fin, aircraft engine), and potentially leading to loss of control and a crash [16–18].

The effect and efficiency of nSDBD-based de-icing on aircraft wings were confirmed in an early experiment [19] in 2016. Later, the concept of plasma-assisted anti-icing or icing control was proposed [20, 21] and a rich set of experiments were conducted [22–34] in the following years. It was found that at the same total power input, an acSDBD has a better anti-/de-icing performance in comparison to a conventional electrical film heater if a duty-cycle modulation [23, 28] is used. The temperature distributions of acSDBDs and nSDBDs were studied using an infrared (IR) thermal imaging system [26, 27]; the authors claimed that heat dissipation for nSDBDs is more effective than for acSDBDs, suggesting better anti-icing performance. An nSDBD has the unique feature of fast temperature increase in the time scale of nanoseconds before V–T relaxation (fast gas heating, FGH) [6, 8, 35], but it is not yet known whether FGH is the main heating source in anti-icing experiments. Further nSDBD-based plasma-assisted anti-icing experiments have been conducted in static air and in icing wind tunnels by different groups [27, 31–33, 36, 37]. It was found that nSDBDs take effect under certain combinations of icing conditions and discharge parameters [27, 37].

Despite the increase in experimental studies, there is little theoretical analysis or numerical modeling devoting to the detailed mechanisms and underlying physics from the perspective of plasma physics. A theoretical analysis of the heat transfer process and heating efficiency is available in paper [27], but this is not linked to detailed experiments or numerical simulations due to a lack of data in the mathematical system. A numerical investigation was found in paper [38], where a phenomenological gas-heating model built in the paper [5] and an ice-accretion model were combined and tested. A number of key questions still need answering with the help of numerical analysis, e.g.: of gas and solid heating, which is more important? Of acSDBDs and nSDBDs, which is better? What is the mechanism of nSDBD-based plasma anti-icing? To answer these questions, the fundamental discharge and heating processes have to be understood.

The present work studies an nSDBD in the anti-icing configuration using a two-dimensional multi-physics model and existing experimental data. The mechanisms of nanosecond-pulsed plasma anti-icing will be discussed based on the analysis of discharge dynamics and heating processes, and its energy efficiency will also be studied and reviewed together with experimental results.

2. Brief of experiments

This paper is a continuation of the previous paper [37] from the perspective of ‘simulation’ and ‘discharge’. Experimental data extracted from an nSDBD-based plasma anti-icing experiment conducted in a closed-circuit continuous icing wind tunnel are used for model validation. In this section we briefly describe the experimental conditions and results used in this paper; more details of the experiments can be found in [37].

The experiments were conducted in moist air generated by the wind tunnel. The velocity was fixed as $U_0 = 65 \text{ m s}^{-1}$. The temperature (T), median volume diameter (MVD) of the droplet and liquid water content (LWC) are three key factors affecting the icing behaviors [16]. In the experiments, the MVD was fixed as $25 \mu\text{m}$, and the LWC was set as 0.5 g m^{-3} . The performance of nSDBD-based anti-icing was recorded at $T = -15 \text{ }^\circ\text{C}$ and $-5 \text{ }^\circ\text{C}$.

Geometrically, two types of nSDBD-based anti-icing strategies exist in publications: the standard-airflow (or span-wise) configuration [27] and the stream-wise configuration [37]. The standard one has the advantage of combining the effect of flow control, while the stream-wise one is believed to be more flexible if the attacking angle changes frequently. Despite the differences, the two configurations can be studied by the same 2D SDBD model using an exposed electrode–encapsulated electrode–exposed electrode geometry. In this work, the results from a stream-wise nSDBD experiment conducted in our group were used for model validation.

The tested stream-wise nSDBD was fabricated on a curved surface and installed on the airfoil, as shown in figure 1(a). The exposed and encapsulated electrodes, made of copper foil, are 2 mm and 10 mm in width, respectively, and 0.06 mm in height. The distance between each exposed electrode is 10 mm. The dielectric is made of Kapton tape with a thickness of 0.3 mm. A homemade power supply was used to produce an 800 ns width pulse at 7 kV and 14 kV peak voltage with 6 kHz frequency. The voltage and current waveforms are measured by a high-voltage probe (Tektronix P6015A), a current probe (Tektronix TCP0030A) and an oscilloscope (Tektronix DPO4104B). The temperature distribution was monitored by a forward-looking infrared (FLIR) thermal imaging camera (SC7300M) with a frame rate of 25 Hz. A Canon 80D camera was used to record the dynamic anti-icing process.

Figures 1(b)–(d) show the experimental results under the three typical icing conditions mentioned above. The figures are captured after 3 min operation: (b) before the icing wind tunnel starts, (c) in moist air with a temperature of $-5 \text{ }^\circ\text{C}$ and (d) with a temperature of $-15 \text{ }^\circ\text{C}$. It can be seen that nSDBD can prevent ice accretion under certain conditions, but not all. In cases of failure, the ice will grow starting from the leading edge, thus preventing icing on the leading edge is the key.

To find the underlying mechanisms of nSDBD-assisted anti-icing, and to reveal the relationship between discharge parameters and anti-icing performances for flexible control, modeling and numerical analysis based on existing experimental data are essential. The following section will illustrate the model used in this work.

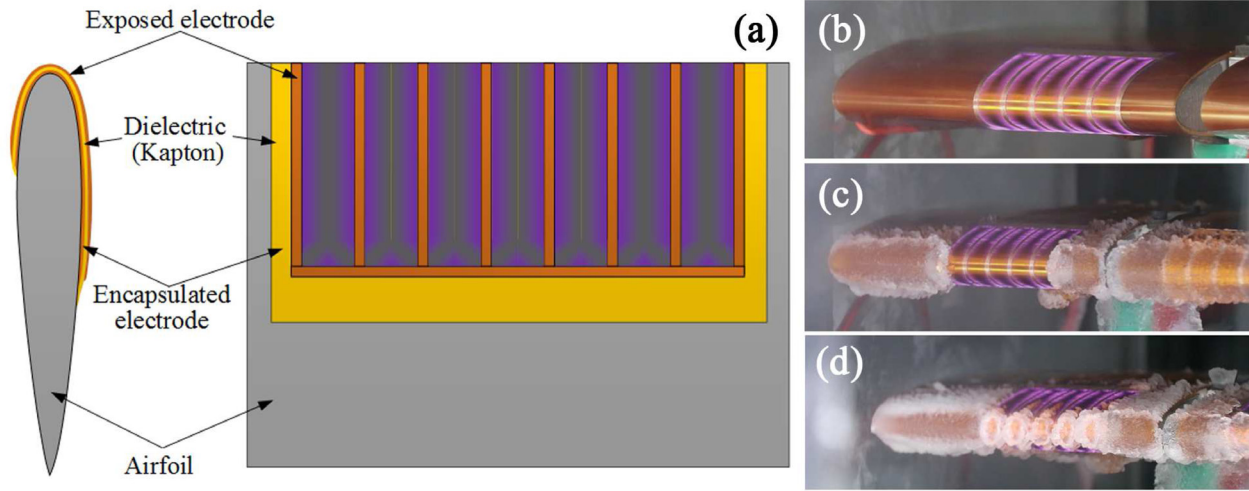


Figure 1. Stream-wise nSDBD: (a) geometric configuration; photos captured by Canon 80D camera in different conditions after 3 min operation: (b) dry air; (c) successful anti-icing; (d) ice accretion over the nSDBD.

3. nSDBD model for anti-icing configuration

PASSKEy (PARallel Streamer Solver with KinEtics) code is used in this work. The numerical approaches, including the code validation in two benchmark cases and comparison with experiments, are presented in detail in [35, 39]. This section simply briefly describes the mathematical model and modifications implemented to the kinetics and heat transfer for the icing conditions.

3.1. Mathematical model

The continuity equations, combined with Poisson's equation and discharge/afterglow chemical kinetics, were solved to describe the behavior of charged, neutral, and excited species and the electric field. The first time the Boltzmann equation for charged species is solved, the neutral species are assumed to be unmovable on the time scale of nanoseconds:

$$\frac{\partial n_i}{\partial t} - \nabla \cdot \mathbf{\Gamma}_i = S_i + S_{ph}, i = 1, 2, \dots, N_{total} \quad (1)$$

$$\mathbf{\Gamma}_i = D_i \nabla n_i + (q_i/|q_i|) \mu_i n_i \nabla \Phi, i = 1, 2, \dots, N_{charge} \quad (2)$$

where Φ is electrical potential, and n_i , q_i and S_i are the number density, charge and source function for species i , respectively. The source function S_i includes gain and loss terms due to gas-phase reactions and is calculated with detailed kinetics, and S_{ph} is the photoionization source term for electrons and oxygen ions. D_i and μ_i are the diffusion coefficient and mobility of charged species, respectively. In the code, $\nabla \cdot \mathbf{\Gamma}_i = 0$ for neutral species is postulated. N_{charge} and N_{total} are the number of charged species and total number of species, respectively.

Photoionization affects the propagation and morphology of surface streamers. An efficient photoionization model based on three-term Helmholtz equations [40, 41] is used to calculate S_{ph} . Despite the presence of water molecules in the system, we still assume that the photoelectrons come from ionization of oxygen molecules by vacuum ultraviolet (VUV) radiation from electronically excited N_2 in $b^1\Pi_u$, $b^1\Sigma_u^+$, and $c^1\Sigma_u^+$ states [42].

Poisson's equation is solved without taking into account the current in the material:

$$\nabla(\epsilon \nabla \Phi) = - \sum_{i=1}^{N_{ch}} q_i n_i - \rho_c \quad (3)$$

where ϵ is the relative permittivity of the dielectric ($\epsilon_d = 3.9$) and gas ($\epsilon_g = 1.0$), and ρ_c is the charge density, satisfying the continuity equation for charges on surfaces:

$$\frac{\partial \rho_c}{\partial t} = \sum_{i=1}^{N_{ch}} q_i [-\nabla \cdot \mathbf{\Gamma}_i]. \quad (4)$$

Finally the system of equations is added with Euler equations:

$$\frac{\partial \mathbf{U}}{\partial t} + \frac{\partial \mathbf{F}}{\partial x} + \frac{\partial \mathbf{G}}{\partial y} = \mathbf{S} \quad (5)$$

$$\mathbf{U} = \begin{bmatrix} \rho \\ \rho u \\ \rho v \\ e \end{bmatrix}, \mathbf{F} = \begin{bmatrix} \rho u \\ p + \rho u u \\ \rho u v \\ (e + p)u \end{bmatrix}, \mathbf{G} = \begin{bmatrix} \rho v \\ \rho u v \\ p + \rho v v \\ (e + p)v \end{bmatrix}, \mathbf{S} = \begin{bmatrix} 0 \\ 0 \\ 0 \\ S_{heat} \end{bmatrix} \quad (6)$$

where ρ is total density of air, u and v are the velocities in two dimensions, and e is the specific total energy. The reactive Euler equations are closed by the equation of state:

$$p = (\gamma - 1) \rho i \quad (7)$$

where $i = e - (u^2 + v^2)/2$ is the specific internal energy.

The FGH energy is calculated from kinetics equations and used as the source term S_{heat} in equation (6). The calculated density, pressure and temperature from the Euler equations are in turn used to update the reduced electric field, Helmholtz equations and kinetics.

3.2. Modifications for water addition

The presence of water requires modifications to the model. Water is available in the system in two states: gas vapor and liquid droplets.

Table 1. Added reactions for FGH in nSDBD in presence of water vapor.

No.	Reaction	Rate constant ^(a)	Reference
R1	$e + \text{H}_2\text{O} \rightarrow e + e + \text{H}_2\text{O}^+$	$f(\sigma, E/N)$	[45]
R2	$e + \text{H}_2\text{O} \rightarrow e + \text{H} + \text{OH}$	$f(\sigma, E/N)$	[45]
R3	$e + \text{H}_2\text{O} \rightarrow e + \text{O} + \text{H}_2$	$f(\sigma, E/N)$	[45]
R4	$e + \text{H}_2\text{O} \rightarrow \text{H}^- + \text{OH}$	$f(\sigma, E/N)$	[45]
R5	$e + \text{H}_2\text{O} \rightarrow \text{OH}^- + \text{H}$	$f(\sigma, E/N)$	[45]
R6	$e + \text{H}_2\text{O} \rightarrow \text{H}_2 + \text{O}^-$	$f(\sigma, E/N)$	[45]
R7	$e + \text{N}_2 \rightarrow e + \text{N}_2(\text{a})$	$f(\sigma, E/N)$	[48, 50]
R8	$\text{H}_2\text{O}^+ + e \rightarrow \text{OH} + \text{H}$	$3.8 \cdot 10^{-7}$	[49, 51]
R9	$\text{H}_2\text{O}^+ + e \rightarrow \text{H}_2 + \text{O}$	$1.4 \cdot 10^{-7}$	[49, 51]
R10	$\text{H}_2\text{O}^+ + e \rightarrow \text{H} + \text{H} + \text{O}$	$1.73 \cdot 10^{-7}$	[49, 51]
R11	$\text{H}_2\text{O}^+ + \text{O}^- \rightarrow \text{H}_2\text{O} + \text{O}$	$4.0 \cdot 10^{-4}$	[49, 51]
R12	$\text{H}_2\text{O}^+ + \text{O}_2^- \rightarrow \text{H}_2\text{O} + \text{O}_2$	$4.0 \cdot 10^{-4}$	[49, 51]
R13	$\text{O}_2^- + \text{H} \rightarrow \text{HO}_2 + e$	$1.2 \cdot 10^{-9}$	[52, 53]
R14	$\text{O}_2^- + \text{H} \rightarrow \text{OH}^- + \text{O}$	$1.5 \cdot 10^{-9}$	[52, 53]
R15	$\text{H}^- + \text{H}_2\text{O} \rightarrow \text{OH}^- + \text{H}_2$	$3.8 \cdot 10^{-9}$	[53, 54]
R16	$\text{H}^- + \text{H} \rightarrow \text{H}_2 + e$	$2.0 \cdot 10^{-9}$	[53, 55]
R17	$\text{H}^- + \text{O}_2 \rightarrow \text{HO}_2 + e$	$1.2 \cdot 10^{-9}$	[53, 56]
R18	$\text{OH}^- + \text{H} \rightarrow \text{H}_2\text{O} + e$	$1.4 \cdot 10^{-9}$	[52, 53]
R19	$\text{OH}^- + \text{O} \rightarrow \text{HO}_2 + e$	$2.0 \cdot 10^{-6}$	[53, 56]
R20	$\text{N}_2(\text{a}) + \text{O}_2 \rightarrow \text{N}_2(\text{v}) + \text{O} + \text{O}(\text{1D}) + 0.89 \text{ eV}$	$2.8 \cdot 10^{-11}$	[48]
R21	$\text{O} + \text{HO}_2 \rightarrow \text{OH} + \text{O}_2(\text{v}) + 1.54 \text{ eV}$	$2.7 \cdot 10^{-11}$	[49, 57]
R22	$\text{OH} + \text{O} \rightarrow \text{O}_2(\text{v}) + \text{H} + 0.51 \text{ eV}$	$2.4 \cdot 10^{-11}$	[49, 57]
R23	$\text{O}(\text{1D}) + \text{H}_2\text{O} \rightarrow \text{OH} + \text{OH} + 0.86 \text{ eV}$	$2.2 \cdot 10^{-10}$	[49, 57]
R24	$\text{N}_2(\text{a}) + \text{H}_2\text{O} \rightarrow \text{N}_2(\text{v}) + \text{OH} + \text{H} + 2.26 \text{ eV}$	$3 \cdot 10^{-10}$	[49, 54]

^a Rate constants are given in $\text{cm}^3 \cdot \text{s}^{-1}$. The energy release in each reaction is from the work of [48, 49, 53]. E/N , the reduced electric field in unit Td, is defined by $E[\text{V}]/N[\text{m}^{-3}] \times 10^{21}$, with N being the number density of neutral gas.

The saturation pressure P_{ws} of water in moist air can be estimated according to [43]:

$$P_{\text{ws}}[\text{pa}] = 610.78e^{(T[^\circ\text{C}]/(T[^\circ\text{C}]+238.3) \times 17.2694)} \quad (8)$$

where T is the dry-bulb temperature of the moist air. The partial pressure calculated for molecular gas H_2O for atmospheric pressure at -15°C is 191 Pa, thus the percentage of water vapor in cases studied in this work is 0.19%.

The addition of 0.19% water vapor leads to slight changes in the transport coefficients and kinetics. To address these changes, the electron swarm parameters were recalculated with the help of the BOLSIG+ package [44] by taking into account electron impact cross-sections of H_2O [45].

The kinetics scheme used in this work is based on [46]. The original kinetics scheme is a combination of kinetics for the description of streamer propagation [47] and FGH [48] in air, and was validated in paper [35]. Paper [48] concluded that the presence of water molecules in air does not lead to an increase in the fraction of energy converted to gas heating, due to ion-molecular reactions involving H_2O and reactions of dissociative electron-ion recombination of H_3O^+ ions. Paper [49] conducted two-dimensional simulations of streamer discharges in humid air with 0.1% and 2% water vapor using a reduced set of kinetics and calculated the energy released from each reaction up to 3 μs . The results show that with 0.1% water vapor, which is close to the case in this study,

the fractional contribution of FGH is the same as dry air (quenching of $\text{O}(\text{1D})$, $\text{N}_2(\text{B, C})$ and dissociation of O_2). Based on this analysis, the original kinetics scheme is updated by combining the H_2O -related FGH reactions in [49]. The added reactions are listed in table 1.

As well as in a vapor state, water also affects the discharges in the form of droplets. Liquid water can be considered as a dielectric with high permittivity ($\epsilon_{\text{water}} \approx 80$). In experiments the water droplets will flow together with the inflow and staggered on the airfoil front. We take a finite region on the leading edge to make an estimation. During the time interval between pulses, the layer thickness of the accumulated liquid water on the finite region can be calculated according to velocity, LWC and f :

$$h_{\text{liquid}} = \text{LWC} \times U_0 / \rho f \quad (9)$$

where $\text{LWC} = 5 \times 10^{-4} \text{ kg m}^{-3}$, $U_0 = 65 \text{ m s}^{-1}$, $f = 6 \text{ kHz}$, and $\rho = 10^3 \text{ kg m}^{-3}$. Equation (9) gives $h_{\text{liquid}} = 5.4 \text{ nm}$. Taking the capacitance of the dielectric $C \sim \epsilon/d$, the capacitance of the water film formed between each pulse would be about $(\epsilon_{\text{water}}/\epsilon_{\text{dielectric}}) \times (d_{\text{dielectric}}/d_{\text{water}}) \approx 10^7$ times the capacitance of the dielectric, thus the total capacitance calculated from $C^{-1} = \sum C_i^{-1}$ indicates that there is almost no influence when water droplets attach to the airfoil surface. Despite the tiny influence of the water film on the discharge, it is interesting to note that $h_{\text{liquid}} = 5.4 \text{ nm}$ is within the range

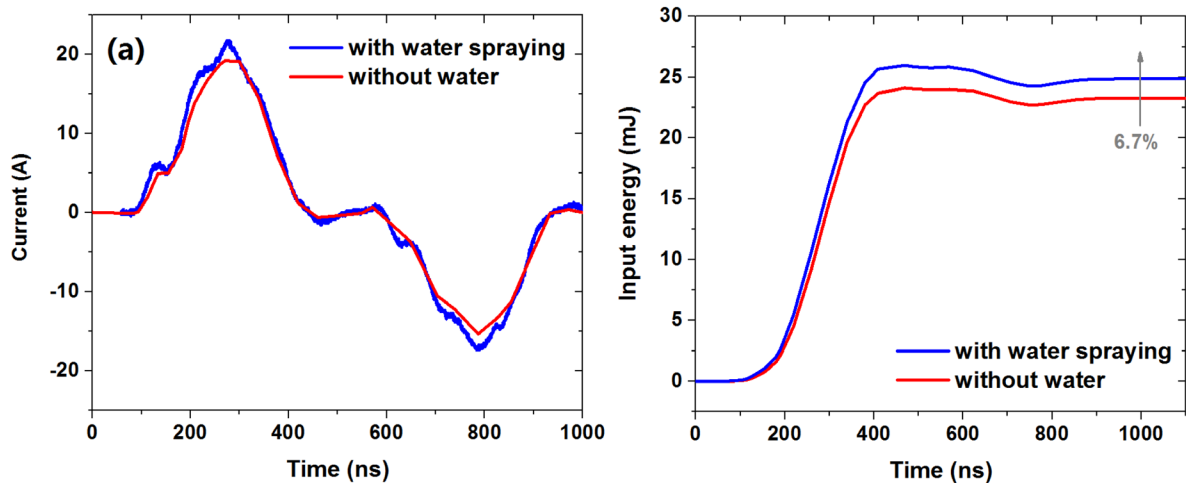


Figure 2. Experimental measurements of (a) electric current, measured with and without water spraying in the wind tunnel; (b) deposited energy of one pulse, calculated by integration of the product of voltage and current.

of depth that plasma in gas could penetrate into liquid water [58, 59]. If the liquid water film changes into solid-state ice, the thickness would increase slightly to 6.0 nm.

We measured the voltage–current curves to determine the influence of the presence of water on the discharge in the icing wind tunnel. With the same voltage input, the discharge current in the presence of sprayed water increased by 3% on average, leading to a 6.7% increase in total energy deposition, as shown in figures 2(a) and (b). This is caused by the effects of possible signal noises and the change of permittivity in the discharge region due to the presence of water. Nevertheless, the above analysis and the tiny experimental difference indicate that water in liquid state in this study does not cause significant differences to the discharge itself.

3.3. Modifications for solid heating

As mentioned previously, between the exposed and encapsulated electrodes there is a solid layer (dielectric and a thin layer of ice). The heating of solid material is an important feature of SDBD, and many groups [15, 22, 37] have monitored the temperature using IR cameras. The experimental results are usually obtained on time scales from hundreds of milliseconds to several minutes, but the heating process starts immediately after discharge. It is not yet clear whether or not the emission collected by the IR camera comes from the gas or dielectric.

The temperature increase in the dielectric may be caused by heat convection from the gas discharge region, a hysteresis phenomenon, or direct ion bombardment. An example is presented in figures 3(a) and (b). We conducted a mini experiment using two IR cameras with 25 and 1000 Hz time resolution. Figure 3(a) is captured 40 ms after one pulse in dry air; there is a diffusive heated region with a temperature increase of 0–2 K. Figure 3(b) is taken 1 ms after the first discharge pulse; the filament structure indicates that the heating may originate from the discharge region or from the dielectric bombarded by the ions in the streamers.

Rodrigues *et al* [15] concluded that for voltages above the breakdown voltage, gas heating is responsible for the majority

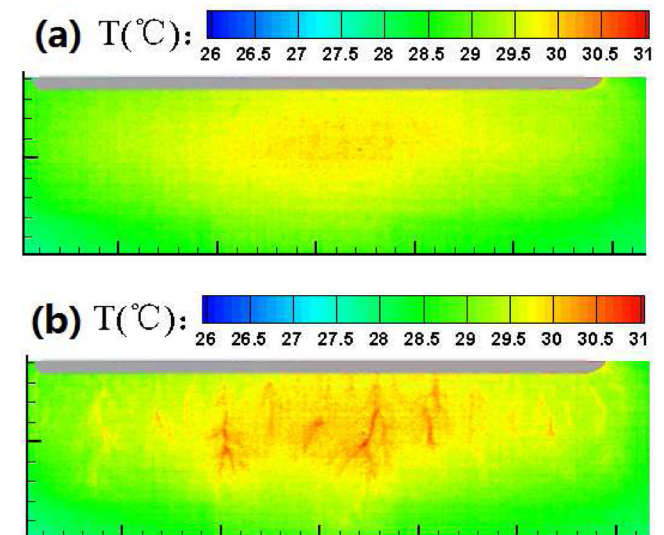


Figure 3. Comparison of IR images captured by IR thermal imaging systems with different time resolutions: (a) 40 ms and (b) 1 ms. The upper grey rectangle represents the exposed electrode.

of the consumed thermal power. In an nSDBD, the voltage rises rapidly above the breakdown voltage at the beginning of the pulse, and thus dielectric heating caused by a hysteresis phenomenon can be neglected. In this work we will discuss the heat contribution from the discharge region: convection and ion bombardment on the time scale of one duty cycle.

It should be mentioned here that the ~ 5 nm ice layer and ~ 0.1 mm dielectric layer were not modeled separately, for the following reasons: (i) the aim of this work is to qualitatively study the influence of different heating sources on the solid region and to provide evidence for mechanism analysis; and (ii) to obtain the complete information, additional changes, including a much smaller mesh (from μm to nm) and additional phase changing processes, are required, leading to additional work that goes beyond the scope of this study.

To quantify the heating of the solid region, the heat transfer equation is solved for the solid material:

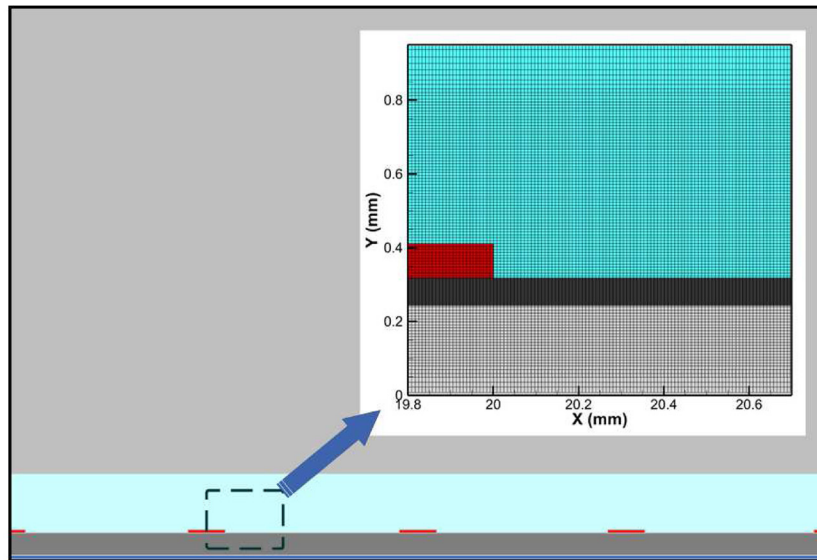


Figure 4. Computational domain and mesh distribution (units in mm) for different equations. Transport equations: light blue domain; Poisson's equation and Helmholtz equation: entire domain; Euler equations: light blue and grey domains; solid heat transfer equations: dark grey domain.

$$\rho_{solid} C \frac{dT}{dt} - \nabla \cdot (\nabla(kT)) = 0. \quad (10)$$

The heat capacity and mass density of the dielectric are $1090 \text{ J mol}^{-1} \cdot \text{K}$ and $1.42 \times 10^3 \text{ kg m}^{-3}$, respectively.

3.4. Geometries, initial/boundary conditions and validations

A computational domain of size $5 \text{ cm} \times 5 \text{ cm}$ was used in the PASSKEY code, and five electrodes were distributed uniformly above the dielectric to reproduce the configuration used in experiments in [37], as shown in figure 4. A uniform Cartesian mesh was used. A mesh size of $8 \mu\text{m}$ was assigned for the plasma region. In the adjacent-to-plasma region of solid (dielectric) the mesh was refined to be $1 \mu\text{m}$. The mesh size of the exposed electrode was not specifically defined; the electrode does not cover the main anti-icing region, and the contact area with the plasma is too small.

The details of the boundary conditions in the PASSKEY code of the Poisson equation, Helmholtz equations and continuity equations are described in [35]. An isothermal boundary condition was defined for the heat transfer equation of a solid. The solid-gas interface was set based on the assumption of ion bombardment and thermal conduction.

The fluid model incorporated in the PASSKEY code does not solve for ion energy flux; thus in this work, to estimate the effect of ion bombardment, we assume the total energy stored in ions $W_{ion} = J_{ion} \cdot E$ in the last plasma mesh nodes at the interface was transmitted to the adjacent solid nodes immediately, i.e. all ions in the last mesh adjacent to the solid will collide with the solid and transfer all the energy to it. The thermal energy flux in the gas can be calculated by Euler equations and then flow into the solid, assuming that $\nabla \Gamma_{thermal} = 0$.

The initial condition was given by setting a background electron density of 10^4 cm^{-3} across the entire plasma region. The previously used initial 'Gaussian plasma spot' near the

edge of the electrode for modeling nanosecond-pulsed discharges was not used in this work, because the voltage rising time in this work ($\approx 300 \text{ ns}$) is much longer than in the previous case ($2\text{--}3 \text{ ns}$), so the artificial plasma spot will cause unphysical current jumps.

Code validations were conducted in addition to the existing benchmark cases presented in [35]. The conditions in an icing wind tunnel are not appropriate for time-resolved spectroscopy diagnosis. The best data available for direct comparison is discharge current. Note that the voltage probe and current probe were not positioned at the same point; there were tens of nanoseconds of shift on the time axis.

The time shift can be corrected by reducing the maximum voltage below the breakdown threshold, and overlapping the current with the time derivative of voltage [60]. We conducted this procedure and found that the calculated discharge currents at two voltage pulses agree well with experimental measurements, as shown in figure 5.

3.5. Coupling of physics and scales

Plasma-assisted anti-icing is a multi-phase, multi-physics and multi-scale problem. The studied system in this work includes gas (air with water vapor), solid (ice and dielectric) and liquid (water drops). In this work the phase change is not considered; the modifications for solid phase and water vapor have been introduced in sections 3.2 and 3.3. In this section we make a brief summary of the coupling strategies for the multiple physics and time scales. A schematic is shown in figures 6 and 7. The details and rationale of the strategies will be given together with the results in the following sections.

The aim of coupling between plasma and fluid is to have a feedback from fluid to plasma and vice versa, thus the same time step and mesh size as in plasma were used. The Euler and plasma equations were calculated together in every time step, and coupled through the exchange of gas density and FGH

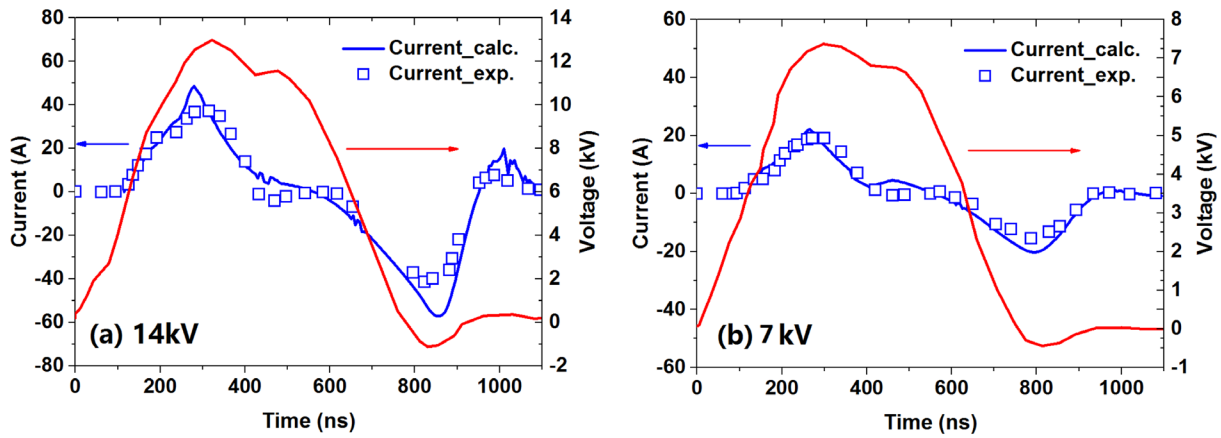


Figure 5. Comparison of measured and calculated discharge current at (a) 14kV peak voltage; (b) 7kV peak voltage. The pulse with 7kV peak value is studied in the following sections.

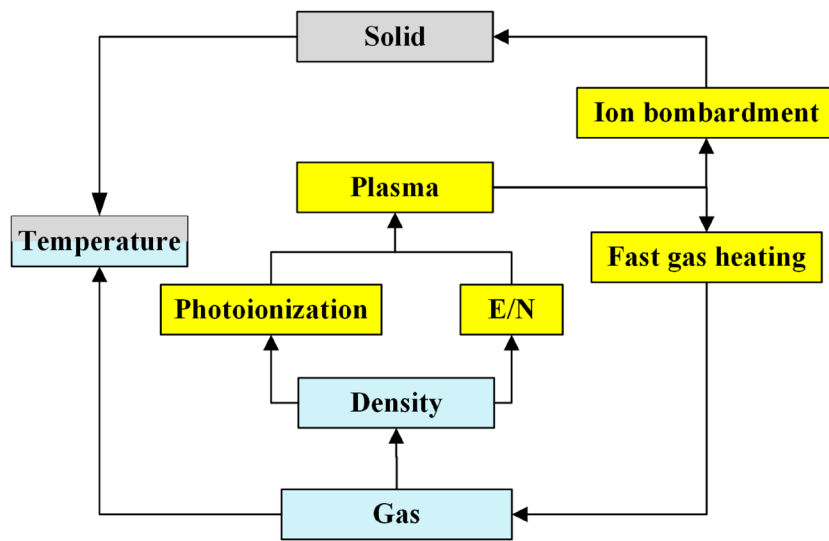


Figure 6. Schematic of multi-physics coupling strategy.

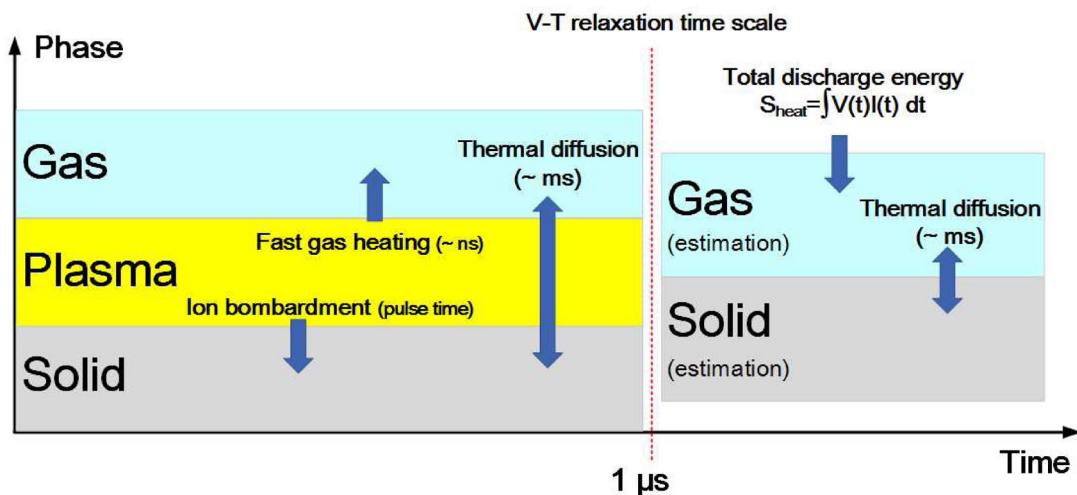


Figure 7. Schematic of multi-scale coupling strategy.

power source. The solid was coupled with the plasma through ion bombardment and with gas through thermal diffusion, as is shown in figure 6.

In each time step, the FGH energy was calculated together with the kinetics equations, and used as a source term for the

gas energy conservation equation (6) in the next time step. The ion bombardment energy was calculated with the transport equation for ion flux, and used as the heat flux source of the solid boundary. Updated gas density was used to calculate E/N , and the photoionization model. When the plasma and

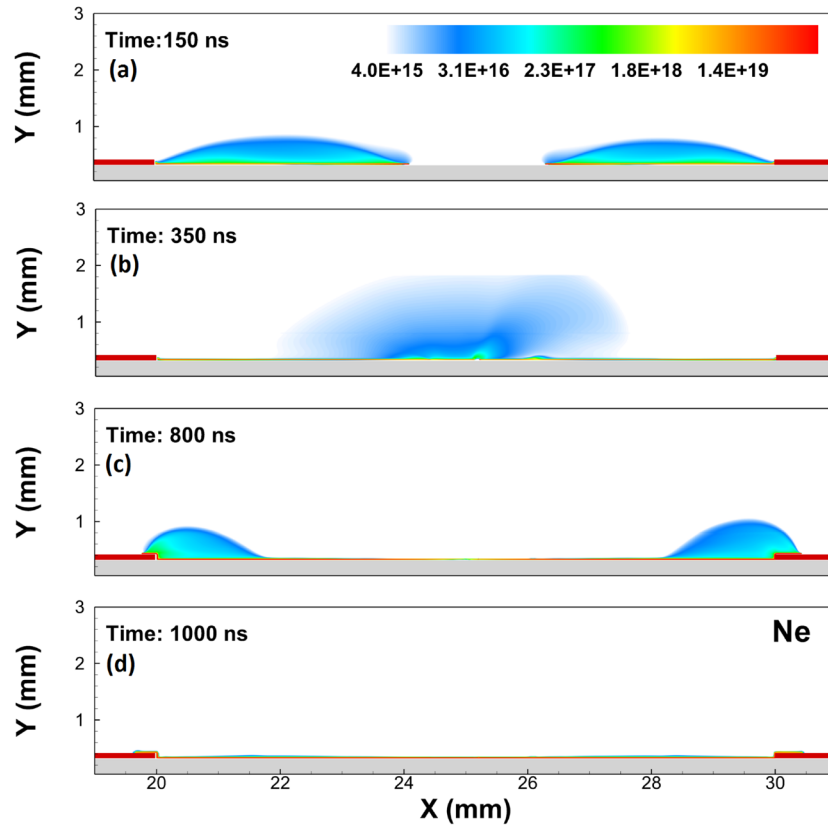


Figure 8. Evolution of electron density under a pulse of 800 ns width at four typical moments. Units in m^{-3} .

fluid were calculated together, the fluid velocity was solved in fluid equations but not coupled into the flux term of the plasma equation (1), (i) to reduce the non-linearity of problem and (ii) because the velocity of the fluid on a nanosecond time scale would have a tiny effect on discharge features.

The physics were coupled on different time scales, as shown in figure 7. FGH energy comes mainly from the fast quenching of excited N_2 and O atoms, and at atmospheric pressure the time scale is tens to hundreds of nanoseconds. Ion bombardment happens when a high electric field exists during the discharge stage. Although thermal diffusion has a much longer time scale (microseconds to milliseconds), the plasma and fluid equations are coupled directly (to calculate temperature rise) in the code, and thermal diffusion is also calculated during discharge. Thus, during a voltage pulse (0–1000 ns) three physics are solved simultaneously with the same time step and mesh in each time step.

On longer time scales ($\geq 1 \mu\text{s}$), the kinetics scheme is no longer accurate due to the absence of vibrational–translational relaxation chemistries, so we only calculated equations (5)–(7) for fluid and equation (10) for solid to estimate the upper limit of the temperature rise in one duty cycle ($\sim 160 \mu\text{s}$). The heating source term for the fluid dynamics equations was recalculated from the measured total energy deposition (integration of voltage and current in figure 5) and averaged over the discharge region calculated in the first $1 \mu\text{s}$. Plasma dynamics is not studied on such a long time scale and the temperature rise calculated from this method is obviously an overestimation; nevertheless, it gives a brief insight into the upper limit of heating performance of this nSDBD, and is still very useful

in supporting the analysis of the anti-icing mechanism, which will be shown in section 4.2.

4. Results and discussion

4.1. Discharge evolution and merging

Gas discharge is the first stage in the nSDBD-based anti-icing application. We traced the evolution of discharge over the pulse duration, and plotted the electron density and electric field at four typical moments: current jump (150 ns), pulse plateau (350 ns), negative pulse (800 ns) and end of pulse (1000 ns) in figures 8 and 9.

Two streamers with the same polarity propagate from the electrode edges toward each other. The electron density in the main body of the streamer is of the order of 10^{18}m^{-3} with a peak density of the order of 10^{20}m^{-3} near the dielectric (figure 8(a)). The electric field is high in the ionization head and near the electrodes (figure 9(a)).

During the plateau of the pulse, the voltage slightly decreases, the electric field on the dielectric increases due to charge accumulation (figure 9(b)), and the electron density near the electrodes decreases. In the gap center, the plasma bulk is sustained due to the electric field induced by surface charge, as can be seen in figure 8(b). The density distribution is symmetric.

Starting from 500–600 ns, the voltage drops rapidly below 0, the electric field in the gap reverses (figure 9(c)) in the direction from the gap center to the electrodes, and negative streamers appear (figure 8(c)) near the electrodes

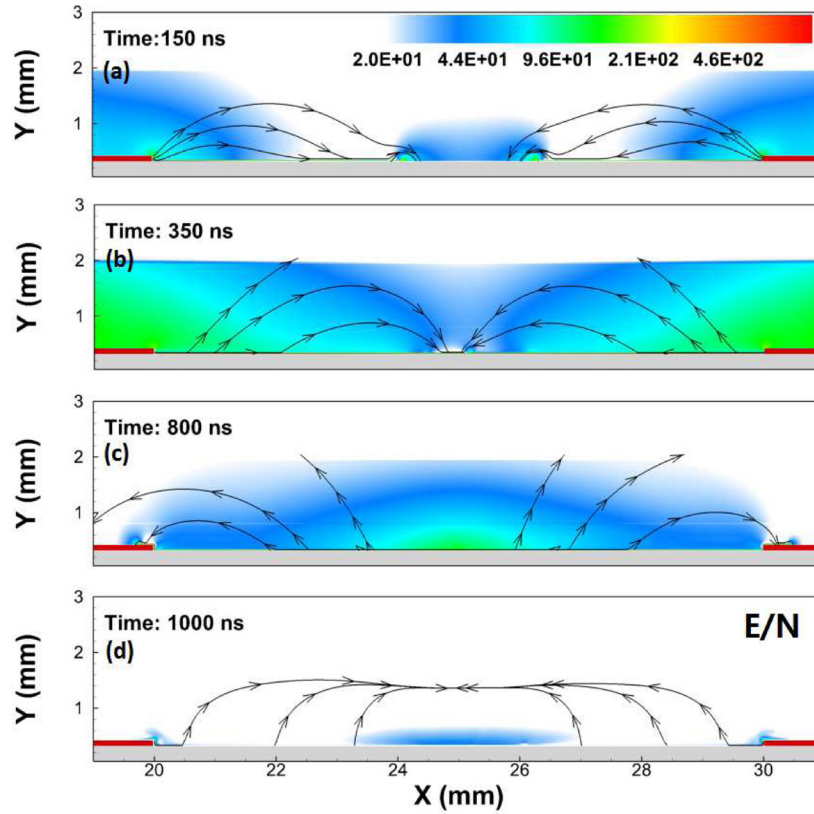


Figure 9. Evolution of reduced electric field under a pulse of 800 ns width at four typical moments. Streamlines are added for each figure. Units in Td.

and propagate to the center. The length of the negative streamer $L_{neg} = 0.2$ c, agrees with the approximation formula $L_{neg} \approx V_{peak}[\text{kV}]/32[\text{kV cm}^{-1}]$, where $V_{peak} = 7$ kV is the peak voltage and 32 kV cm^{-1} is the threshold field of ionization for air at atmospheric pressure.

At the end of the pulse, the voltage rises from -0.5 kV to 0 , causing the electric field to reverse again (figure 9(d)). A weak discharge starts near the electrodes ((figure 8(d))), leading to a jump in current value as shown in figure 5(b).

An interesting question with practical implications is: in the anti-icing configuration, will the counter-propagating surface streamers merge or will the two ionization heads stop somewhere, leaving an unheated region in the middle? What is the key factor affecting this phenomenon?

For a standard ‘airflow’ configuration, the length of the discharge region is dominated by the positive-polarity streamer, which is at least 2–3 times the distance of a negative streamer under the same voltage [35], that is, 0.4–0.6 cm in this work. More precisely, a recent analytical estimation [61] reveals that the length of a positive surface streamer L_{pos} is a function of peak voltage V_{peak} during discharge:

$$L_{pos} \approx \frac{2h_d v_{ic} V_{peak}}{K_e E_c^2} \quad (11)$$

where $h_d = 50 \mu\text{m}$ is the thickness of the streamer, $v_{ic} = 3.5 \times 10^{-11} \text{ s}^{-1}$ is the reduced ionization frequency, $K_e = 600 \text{ m}^2 \text{ V}^{-1} \text{ s}^{-1}$ is the electron mobility and $E_c = 277 \text{ kV cm}^{-1}$ for an atmospheric surface streamer.

Substituting the experimental voltage $V_{peak} = 7$ kV into equation (11) gives $L_{pos} \approx 0.53$ cm. This L_{pos} value is just half

the electrode distance, so ideally the two streamers could just cover the entire gap. To check the behavior of the two counter-propagating streamers at this critical condition, we plot the evolution of electric field vectors at the approaching moments in figure 10.

The characteristic propagation time of a surface streamer is in the range of 2–10 ns; however, figure 10 indicates clearly that the streamers are still propagating 60 ns after ignition. As the streamers approach, the propagation velocity of each streamer decreases dramatically from the order of mm/ns to $40 \mu\text{m ns}^{-1}$, the electric field vectors are directed mainly to the perpendicular surface between the two ionization heads, and with the increase in voltage during propagation, the surface charge deposition from the ionization heads grows. At the end of propagation, the two streamers do not merge, leaving 0.1 mm distance between them.

It should be noted here that the voltage pulse studied in this work is of the order of ~ 800 ns width and only 7 kV in amplitude; the evolution of the discharge parameters is not exactly the same when using an ultrashort nanosecond high-voltage pulse (~ 10 ns) as in [27]. Here we calculated an additional case (‘CASE 2’) using a typical ultrashort pulse generated by a commercial FID Technology pulser (FPG20–03PM/NM) with 24 kV peak voltage, 20 ns pulse width and 2 ns rising time to compare with the previous one (‘CASE 1’).

The evolution of the electron density and reduced electric field of CASE 2 is shown in figures 11 and 12. Both the electron density and electric field are much higher than the case of a longer pulse. It is clearly seen that with an ultrashort voltage, two positive streamers confront each other (figures 11(a) and

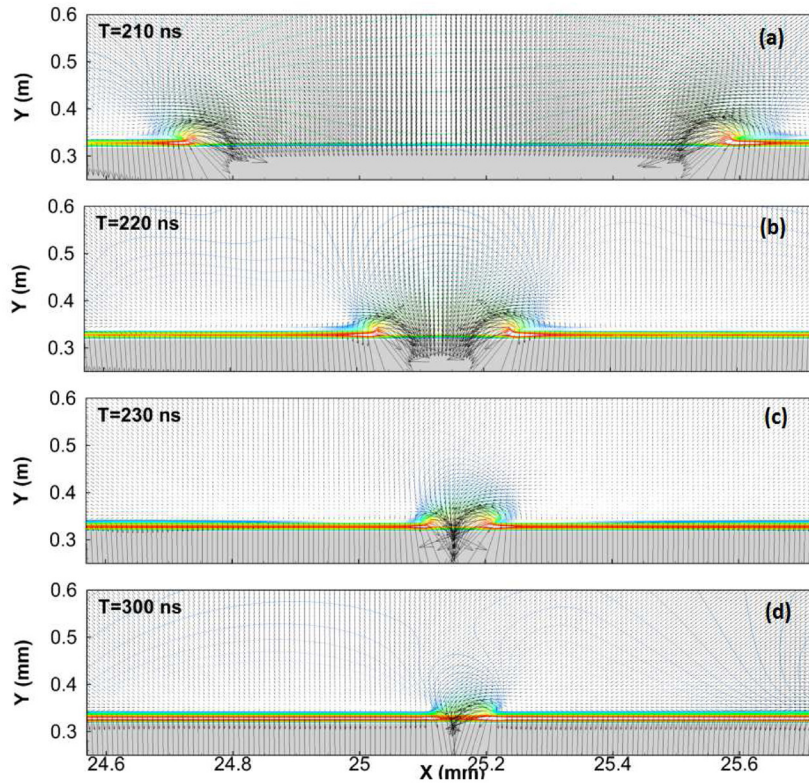


Figure 10. Evolution of electric vectors at moment of streamer approach for $V_{peak} = 7$ kV case. The vector length is linearly proportional to the absolute electric field. The contour color indicates the distribution of the reduced electric field.

(b) during the rising time, merge after 2.5 ns (figure 11(c)), and negative discharges then start before the streamer channel decays (figure 11(d)). The electric field in CASE 2 also has a ‘propagation with ionization head—direction reverse—decay’ process as in CASE 1, but the electric field in the middle of the gap is much smaller (< 20 Td).

If we solve equation (11) for the 24 kV, 2 ns rising time case, we will have $L'_{pos} \approx 1.83$ cm. Thus even a single streamer could cover the entire gap, which is a rather different situation to the 7 kV case. We draw the electric field vectors before and after the moment of approach in figure 13. It can be seen that the two streamers merge within 0.5 ns; the ionization heads disappear, leaving a small region of low electric field caused by residual charges in the gap.

Zooming in on the about-to-touch region for each case gives figures 14(a) and (b), the electron density distribution after the streamers stop. In CASE 1, the streamers are already at the end of the propagation stage when approaching each other, and the appearance of a counter-propagating streamer reduces the discharge length of each streamer. The behaviors of two counter-propagating volumetric streamers have been studied experimentally [62] and numerically [63]; the authors concluded that counter-propagating streamers driven by the same voltage will not merge [63], and with the decrease in potential on the electrode, the electric field between the ionization head will rise, leading to a secondary glow in helium [62]. The phenomenon in CASE 1 is similar to that of volumetric streamers: the streamers slow down initially and stop before merging, and the electric field in

the middle gap is higher when the electrode potential drops (figure 9(c)).

In CASE 2, the two streamers are ‘connected’ after touching, significantly different to CASE 1 and the case of volumetric streamers. This phenomenon is quite counterintuitive, as existing studies have shown that counter-propagating volumetric streamers will not merge/touch. Our explanation is that the counter-propagating volumetric streamers will slow down due to the strong charge layer of the same polarity in another ionization head, but the surface streamer is different to the volumetric one: (1) it is attached to the dielectric, and the charge in the ionization head will be lost on the surface when the two ionization heads approach; (2) the electric field is very strong between the streamer body and the dielectric but much weaker on the upper side, and once the ionization heads disappear it is possible for the two streamers to merge gradually. Figures 10 and 13 show that as the two streamers approach each other, the electric field in the ionization head is directed towards the surface and the strong charge layers are deposited onto the surface; this is very different from the case of volumetric streamers. As a result, the two streamers are finally ‘connected’.

Comparison between the CASE 2, CASE 1 and volumetric counter-propagating cases indicates that: (1) the dielectric surface may play an important role. The electric field in the ionization head is mainly directed perpendicularly to the surface, as is shown in CASE 1. (2) The maximum voltage V_{peak} during discharge propagation may be another influencing factor as it decides the discharge length L_{pos} in nSDBD. If the

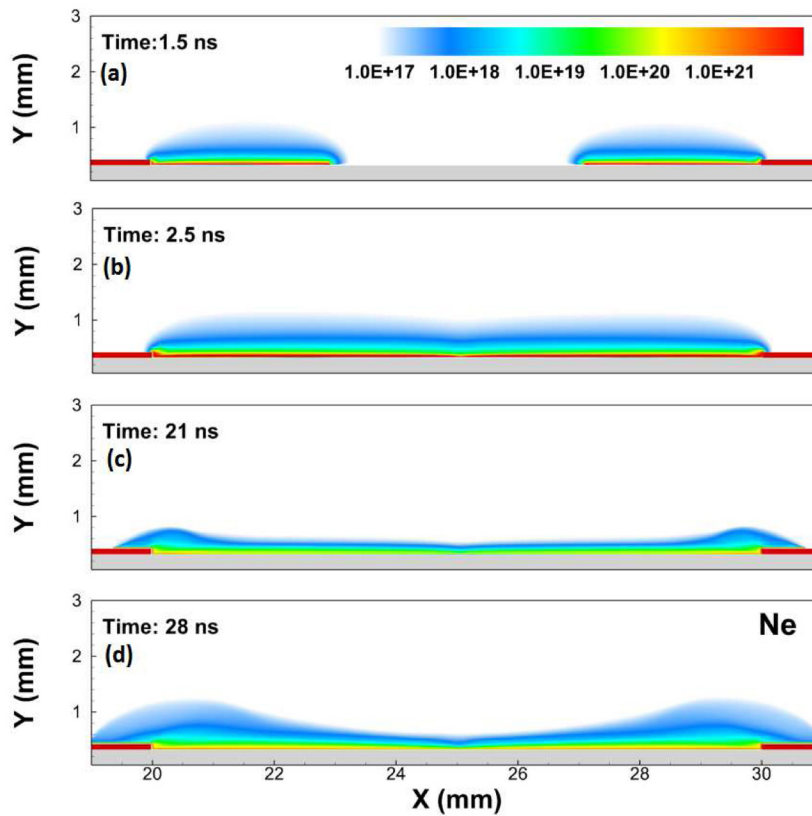


Figure 11. Evolution of electron density under a pulse of 20 ns width at four typical moments. Units in m^{-3} .

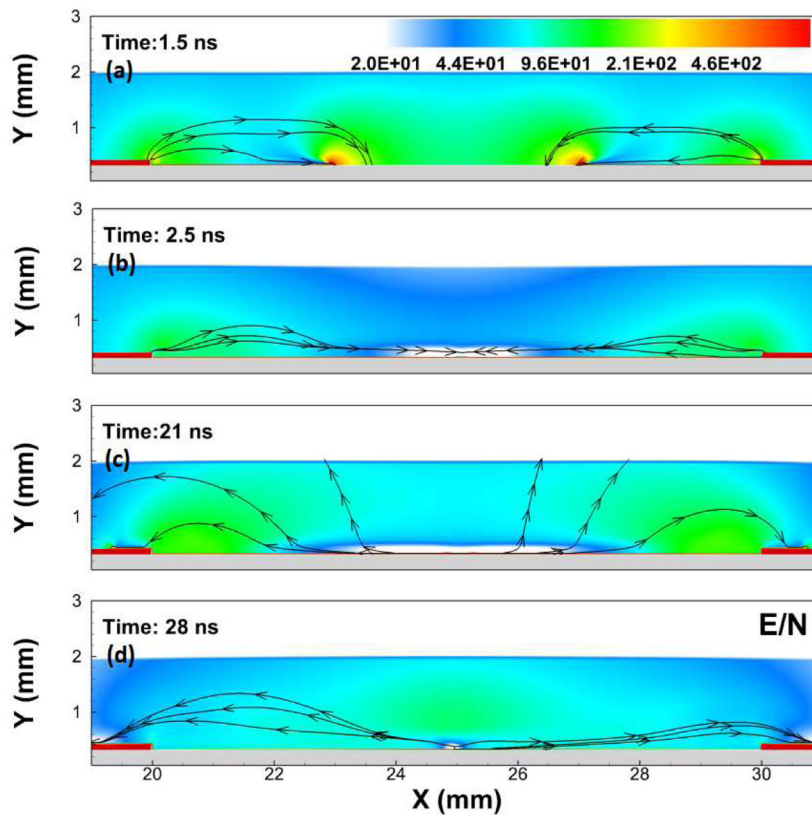


Figure 12. Evolution of reduced electric field under a pulse of 20 ns width at four typical moments. The streamlines are added for each figure. Units in Td.

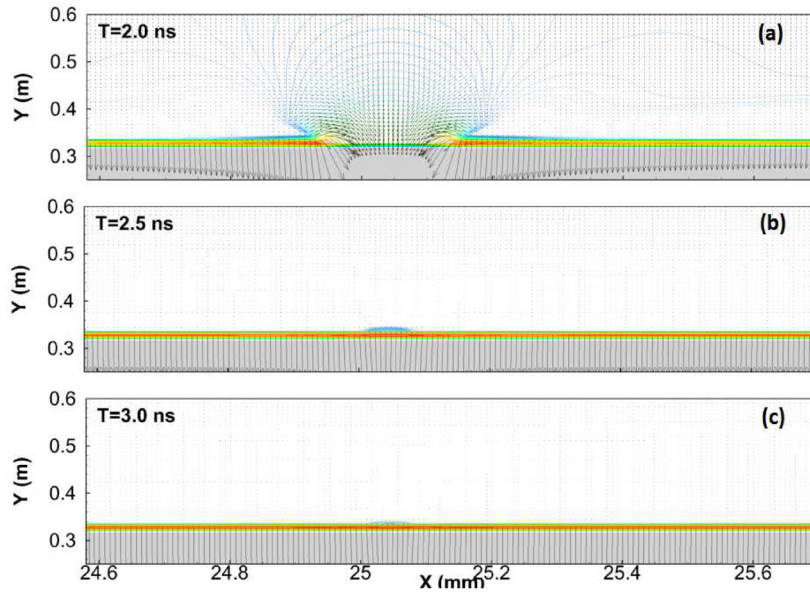


Figure 13. Evolution of electric vectors at moment of streamer approach for the $V_{peak} = 24$ kV case. The vector length is linearly proportional to the absolute electric field. The contour color indicates the distribution of the reduced electric field.

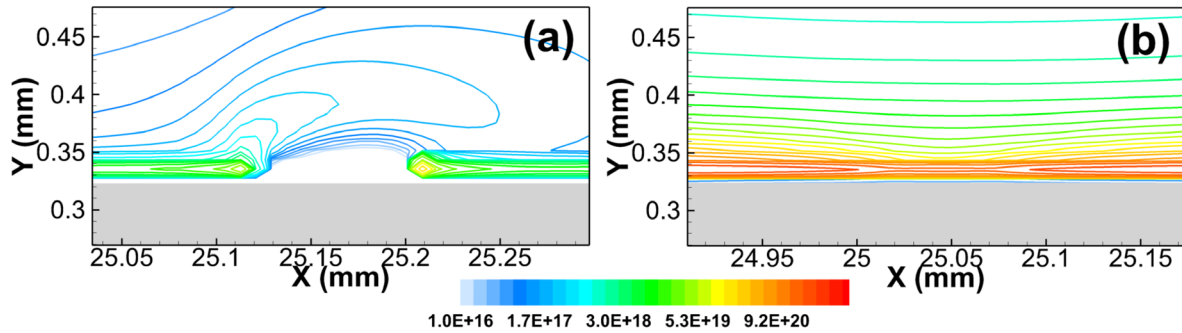


Figure 14. Distribution of normalized electron density when the two streamers stop. The streamers stop in (a) the 7 kV, 400 ns rising time case, and merge in (b) the 24 kV, 2 ns rising time case.

sum of the lengths of the two streamers calculated from equation (11) is significantly larger than the electrode distance, the surface streamers will merge as in CASE 2. Currently we have no experimental results to support or validate this ‘merging’ phenomenon by numerical observation. Such an experiment is out of the scope of the topic of plasma-assisted anti-icing, but it is nonetheless a very interesting topic to be studied in the future.

4.2. Heating of gas and solid

The energy transmitted to discharge will be released into gas through heating. We calculated the temperature rise during the pulse due to FGH and probed four points in the streamer channel. The results are shown in figure 15. The probes are positioned at 0.2, 1.2, 2.2 and 3.2 mm from the exposed electrode, 0.03 mm above the dielectric. The temperature rise can reach a maximum of 30 K in the first 200 ns near the electrode, and then decays due to heat diffusion (figure 15(b)).

The estimated upper limits of temperature rise in static and flowing air at point A are presented in figure 15(c). An important conclusion can be drawn here: the heated

discharge region cannot be kept at experimental airflow velocity (65 m s^{-1}) at the leading edge of the airfoil. In the case of an ultrashort voltage pulse [27], the deposited energy would be smaller and thus the temperature would drop even faster. In other words, the mechanism of nSDBD-based anti-icing does not produce a sustainable heated region above the dielectric.

The role of solid heating in nSDBD for anti-icing applications is still under dispute. Does the IR image in figure 3 exactly represent the solid temperature? What is the role of solid heating in nSDBD-based plasma anti-icing? To answer these questions, we probe the calculated temperature rise 2.5 mm from the electrode, below the surface at different depths (1, 3, 5 and 7 μm), and show the results in figures 16 and 17.

Figure 16 shows the calculated temperature rise due to ion bombardment during the discharge. At the end of the first voltage pulse, the order of temperature rise is 10^{-3} K at several micrometers depth. Obviously, the ≈ 2 K temperature rise in the filaments of figure 3 does not originate from ion bombardment.

Figure 17 shows the estimated upper limit of temperature rise in the solid in one duty cycle in static air and in

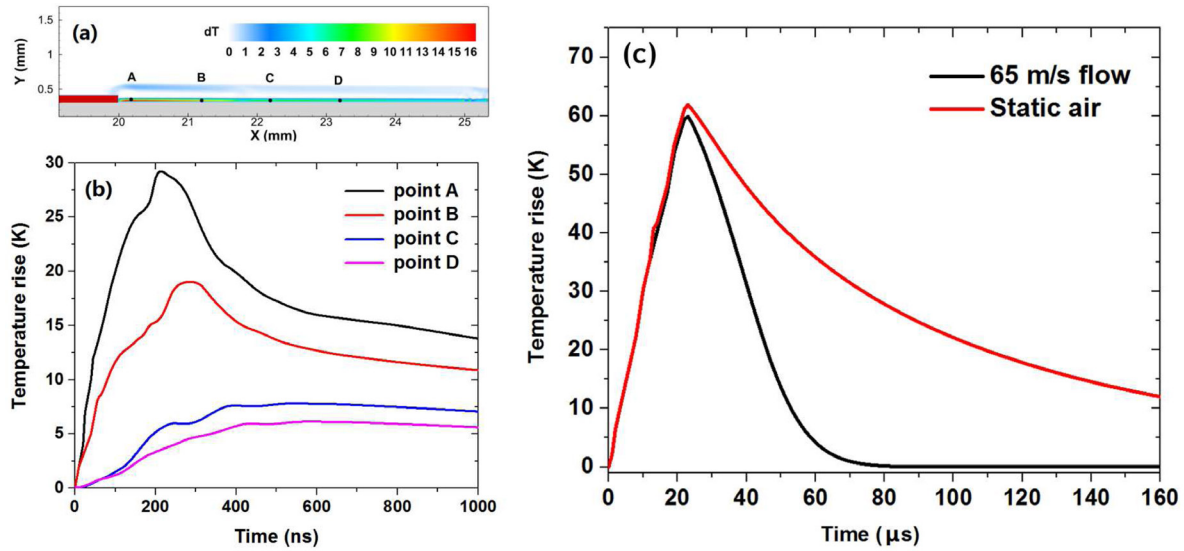


Figure 15. Temperature increase in the gas. (a) Calculated 2D distribution at 800 ns; (b) calculated temporal evolution of temperature increase in one pulse at four points marked in (a); (c) estimated temporal evolution of temperature increase in one duty cycle at point a in case of static air and 65 m s⁻¹ flowing air; the temperature increase is calculated assuming all the deposited energy is transferred to the discharge region uniformly.

experimental air velocity (65 m s⁻¹). The temperature rise caused by heat diffusion from gas is 5–10 times larger than that of ion bombardment. Despite the fact that the results in figure 17 are an overestimation of temperature rise (assuming all deposited energy is transferred into gas) due to thermal conduction, it provides some key information:

- (i) The temperature increase at the end of one duty cycle (160 μs) is not 0, indicating that the energy can be ‘stored’ and accumulated in the dielectric layer at each cycle pulse. Thus, after thousands of duty cycles, the temperature increase could be significant. This thermal accumulation effect may lead to damage of the thin dielectric material after long operation without any cooling methods. In practical applications, specialized materials, smart cooling structures or a modulated discharge scheme are of crucial importance.
- (ii) Thermal conduction is the main mechanism heating the solid, while ion bombardment is much weaker. However, neither thermal conduction nor ion bombardment could explain the ≈2 K temperature rise shown in figure 3. The temperature derived from the IR camera should be the gas temperature at the beginning, and possibly the mixing of gas and solid/liquid temperature at longer time scales.
- (iii) Note that there is a thin layer of supercooled ice/water with thickness 4–5 nm above the dielectric. It is very interesting that the integrated thermal flux over one duty cycle and the energy required for heating the thin ice/water layer up to 0 °C is of the same order. A simple check can be done: assume the heated depth of the solid is only 7 μm, and take the temperature rise at 3 μm depth as an average, estimating the heating energy flow into the solid and only into water film, respectively using:

$$Q \sim \rho C \Delta T \times \text{Depth} \quad (12)$$

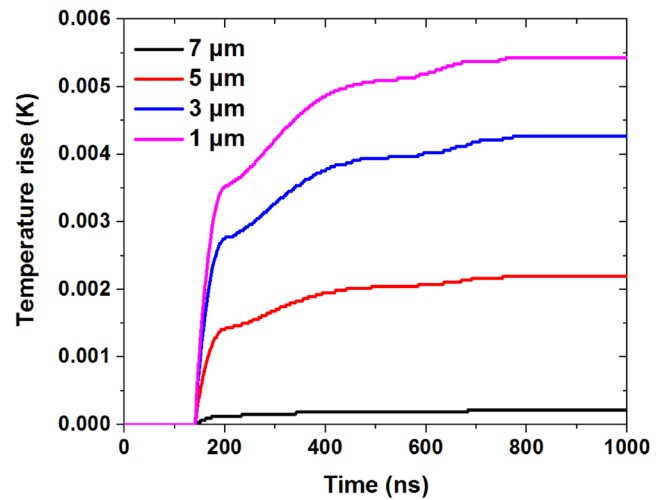


Figure 16. Calculated dielectric temperature increase caused by direct ion bombardment in one pulse at depths of 1, 3, 5 and 7 μm. The attached IR image is for reference.

where for the solid dielectric, $C_s = 1.09 \times 10^3 \text{ J mol}^{-1} \cdot \text{K}$, $\rho_s = 1.43 \times 10^3 \text{ kg m}^{-3}$, $\text{Depth}_s = 7 \times 10^{-6} \text{ m}$ and $\Delta T_s = 0.03 \text{ K}$ for the solid. Equation (12) gives $Q_s \sim 0.33 \text{ J m}^{-2}$ for the solid region. If we substitute $C_w = 4.2 \times 10^3 \text{ J mol}^{-1} \cdot \text{K}$, $\rho_w = 10^3 \text{ kg m}^{-3}$, $\text{Depth}_w = 5.4 \times 10^{-9} \text{ m}$ and $\Delta T_w = 15 \text{ K}$ to calculate for the water film, we will have $Q_w \sim 0.34 \text{ J m}^{-2}$. For ice $C_i = 2.1 \times 10^3 \text{ J mol}^{-1} \cdot \text{K}$, $\rho_i = 0.9 \times 10^3 \text{ kg m}^{-3}$, $\text{Depth}_i = 6.0 \times 10^{-9} \text{ m}$ and $\Delta T_i = 15 \text{ K}$ gives $Q_i \sim 0.17 \text{ J m}^{-2}$.

The above estimation confirms that Q_s , Q_w and Q_i are of the same order, and the thermal flux from the discharge region into the water/ice layer is capable of heating them above 0 °C. This conclusion forms the basis for energy analysis in the following sections.

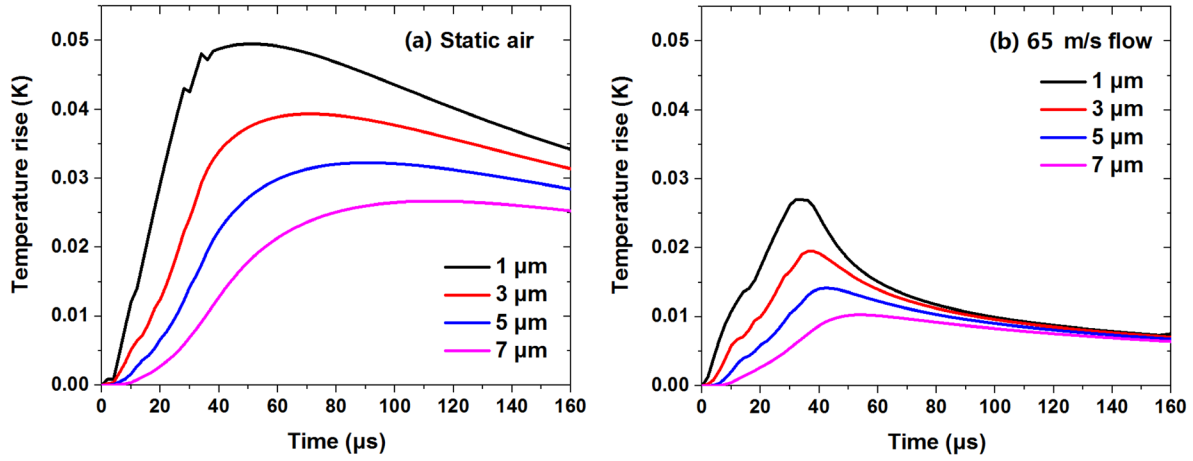


Figure 17. Estimated upper limit of dielectric temperature increase due to heat transfer from gas at depths of 1, 3, 5 and 7 μm in (a) static air and (b) 65 m s^{-1} flowing air.

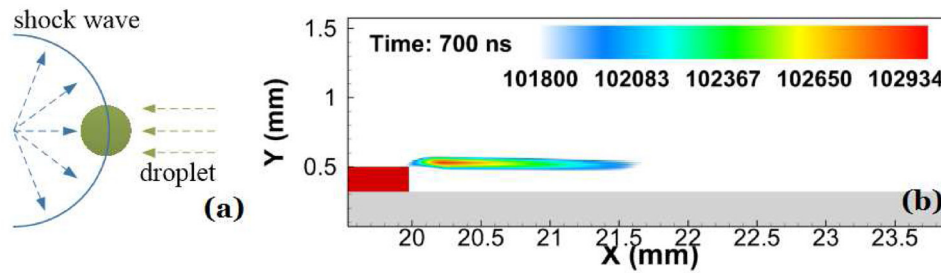


Figure 18. Schematic figure of shockwave–droplet interaction in (a) and the calculated pressure perturbations caused by the ‘micro-shockwave’ in (b); units in Pa.

4.3. Pressure waves and vaporization

There is some dispute over whether or not the ‘micro-shockwave’ generated in an nSDBD [5, 10, 35] works in de-icing/anti-icing applications by repelling the water drops (figure 18(a)), and whether or not the micro-size supercooled water drop could be heated to above $0\text{ }^{\circ}\text{C}$ or vaporized in the heated gas before reaching the dielectric.

The first question can be answered using the modeling results of fluid equations. As shown in figure 18(b), the pressure wave in this work is rather weak: there is a pressure increase of only 500–2000 Pa within the 1.5 mm distance from the electrode in the first 700 ns. The pressure wave then decays soon afterwards. At this level of pressure perturbation, the velocity change Δu on a tiny water drop can be simply calculated by

$$\Delta u = F\Delta t/m = \Delta P S \Delta t/m \quad (13)$$

where the pressure increase $\Delta P = 2000\text{ pa}$, the cross-section of the water drop $S = \pi(MVD/2)^2 \approx 1.56 \cdot 10^{-10}\text{ m}^2$, the mass of water drop $m = \rho \cdot 3\pi(MVD/2)^3/4 = 4.6 \cdot 10^{-12}\text{ kg}$, and the affecting time calculated from the pressure-affected region $\Delta t = 10^{-4}[\text{m}]/65[\text{m/s}] = 1.5 \cdot 10^{-6}\text{ s}$. Substituting into equation (13) we get $\Delta u \approx 0.1\text{ m s}^{-1}$, which is only 0.15% of the water drop velocity. Thus the impact of the ‘micro-shockwave’ could be neglected in anti-icing applications.

For the second question, we estimated the time taken for a 65 ms^{-1} droplet to flow through the heated region ($\approx 0.1\text{ mm}$; see figure 15) is approximately $1.5\text{ }\mu\text{s}$. The discussion

of figures 16 and 17 in the previous section already highlighted that in such a short time (within one duty cycle), the temperature rise of materials with similar thermal characters is only of the order of 10^{-3} K , so the water drops cannot be heated above $0\text{ }^{\circ}\text{C}$.

Another question of interest is: will the droplets reduce in size when traveling in the heated region? The diameter of a supercooled water droplet D at a higher temperature can be calculated according to the ‘square law’ [64]:

$$D^2 = D_0^2 - kt, k = \frac{8\lambda}{\rho_{\text{water}} C_p} \frac{Nu^*}{2} \ln\left(1 + \frac{C_p(T_{\text{amb}} - T_{\text{water}})}{h}\right) \quad (14)$$

where $D_0 = MVD = 25\text{ }\mu\text{m}$ is the original diameter, $\lambda = 2.48 \cdot 10^{-2}$ is the thermal conductivity of air, $\rho_{\text{water}} = 10^3\text{ kg m}^{-3}$ is the water density, $C_p = 4.2\text{ kJ mol}^{-1} \cdot \text{K}$ is the heat capacity of water, $Nu^* = 2 + 0.6\text{Re}^{0.5}\text{Pr}^{0.33}$ is the Nusselt number, $\text{Re} = 4062$ is the Reynolds number of air, $\text{Pr} = 0.7$ is the Prandtl number of air, T_{amb} and T_{water} are the temperatures of the ambient air and the droplet, respectively, and $h = 2256\text{ kJ kg}^{-1}$ is the vaporization latent heat.

The evolution of a single droplet diameter calculated from equation (14) is plotted in figure 19(a). It takes 200–300 μs to achieve total vaporization, much larger than the $1.5\text{ }\mu\text{s}$ heating time. However, if we zoom in on the time scale of discharge pulse 0–225 ns, as shown in figure 19(b), it is interesting to find that it takes only 75–125 ns for the droplet to reduce by 5 nm (corresponding to the maximum thickness of the water

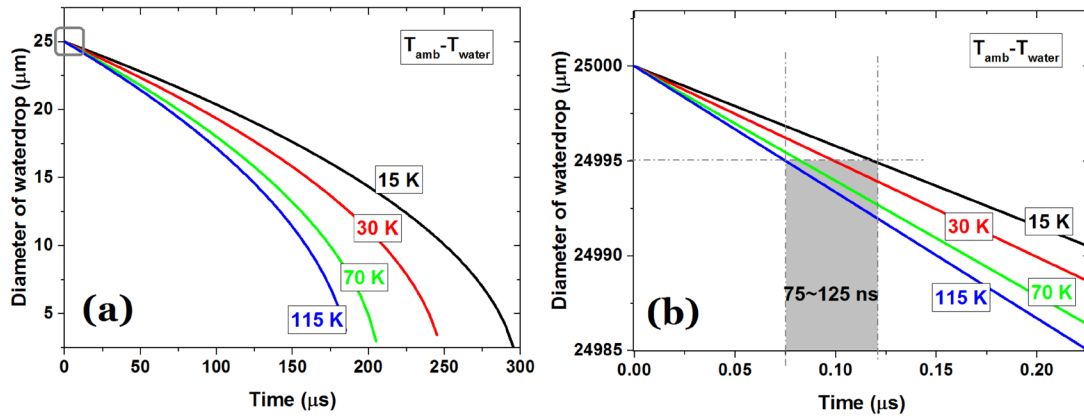


Figure 19. Estimated evolution curves of the supercooled droplet diameter at temperature differences of 15 K, 30 K, 70 K and 115 K in time scales of (a) 300 μs and (b) 0.2 μs at the beginning.

film formed on the surface at the end of each duty cycle; see equation (9). This is additional evidence supporting the conclusion of the previous section: the heat flux from the heated gas directly to the water/ice layer is the main mechanism of nSDBD-based plasma-assisted anti-icing.

4.4. Energy analysis for anti-icing applications

In previous sections we concluded that the heat energy for anti-icing comes directly from heated gas. The time to remove the thin water layer formed on the surface is only tens to hundreds of nanoseconds, thus vibrational-translational relaxation does not dominate. Combination of these two facts indicates that FGH might play a key role in nSDBD-based plasma-assisted anti-icing. In this section, we analyze the FGH energy and anti-icing energy to verify the role of FGH.

Figure 20 shows the calculated total and FGH energy density averaged within the 0–50 μm range above the dielectric. An analytical total energy deposition calculated according to [65, 66] is presented for direct comparison and validation. The fractional ratio $\eta_{FGH} \approx 6\%$ is evaluated by fitting $\eta_{FGH} W_{total,analytical}$ with $W_{FGH,calculated}$.

There is another factor of interest, $\eta = E_{melt}/E_{dep}$, the fractional ratio of anti-icing energy E_{melt} and total deposited energy E_{dep} . The total deposited energy can be calculated by integrating experimental voltage and current, $E_{dep} = \int V(t)I(t)dt$. For E_{melt} , we take a finite surface $L \times W$ on the leading edge of the airfoil (where the icing starts); the energy required to melt the ice film formed in one duty cycle can be evaluated by the following expression [19, 37]:

$$E_{melt} = LWC \cdot \frac{uWL}{f} (C \cdot \Delta T + H) \quad (15)$$

where L is the length of the heating/discharge region of a single streamer, W is the length of the electrode, u is the flow velocity, ΔT is the temperature difference between the ice and 0 °C, and H is the latent heat of fusion required for the ice to change phase.

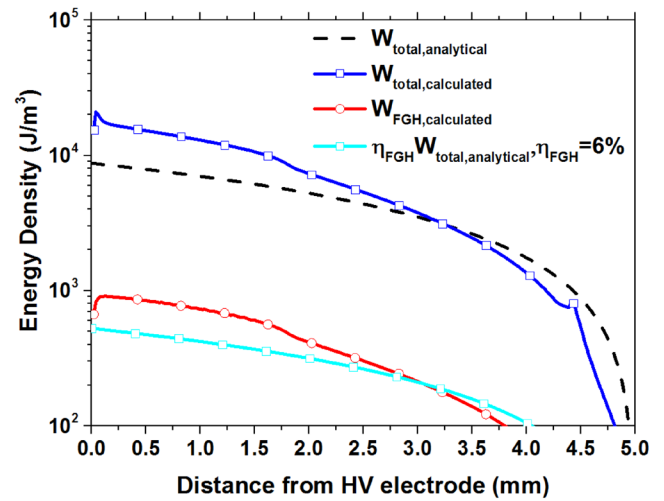


Figure 20. Comparison of density of deposited FGH energy and analytical results calculated from [66] along the streamer direction. The total energy density calculated from [66] was multiplied by the fractional ratio η_{FGH} ; see details in the text.

It should be noted that equation (15) has to be corrected for nSDBD-based anti-icing applications in three aspects:

- (i) To remove the latent heat term H . In [19] this expression is built assuming that ice of a certain mass Δm already forms, while in this work, the supercooled water is either heated/vaporized before icing or melted after icing in each duty cycle, so the latent heat contributes to both gas and solid heating energy. In the previous paper [37], a preliminary calculation taking H into account is conducted, but we later found that the energy deposition per unit length of electrode in that paper is not accurate; the corrected value of η in [37] is about 36%. However, the fraction of discharge energy converted to gas heating in nanosecond discharges does not exceed 30% [48]. This high η value means all the heating energy is devoted to preventing ice formation, which is rather susceptible. Thus, the latent heat term should be removed.

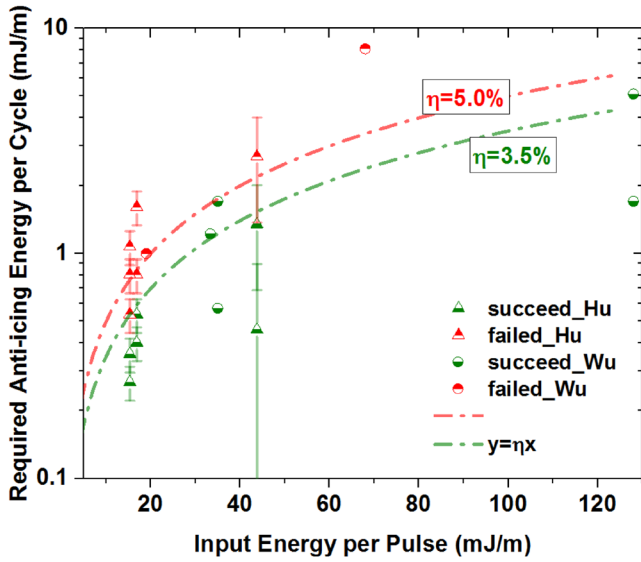


Figure 21. Diagram of input energy per pulse-required anti-icing energy per cycle. The red and green lines are calculated from equation (16), the triangles with error bars are experimental data collected from existing publications [27, 31, 33], and the circles are data from icing wind tunnel experiments conducted in our group. Some results have been presented in paper [37].

- (ii) To normalize with the electrode length W . One unique feature of nSDBD is that the discharge starts almost simultaneously from the electrode, so the parameter variation is small. Thus equation (15) can be normalized by W for convenience of analysis and power supply design.
- (iii) To add corrections for the span-wise nSDBD anti-icing configuration. In some groups the electrode is not positioned at the leading edge, thus it is necessary to add an additional $\cos\phi$ term to account for the angle between the normal of the electrode surface and the flow, ϕ .

Thus equation (15) can be rewritten as:

$$E'_{melt} = LWC \cdot \frac{uL}{f} (C \cdot \Delta T) \cos\phi. \quad (16)$$

We calculated E_{dep} and E'_{melt} from recent publications [27, 31–33, 36, 37] and plotted them as discrete points in figure 21. The red points refer to failed cases, and the green successful cases. The criterion for a ‘failed’ or ‘successful’ case is the existence of an ice-free leading edge; the temperature at the leading edge is the lowest, so if the nSDBD thermal energy is high enough to prevent ice from forming on the leading edge, then it is also enough for other positions (if SDBD is installed there).

For the triangular points in figure 21, there exist some uncertainties: (i) the input energy per pulse (x -axis) is taken directly from the original papers, due to a lack of discharge current data; (ii) the required anti-icing energy per cycle (y -axis) is affected by ϕ , and to find this value we need the exact position of the SDBD nearest to the leading edge, but this is not explicitly presented. The lack of a ϕ value leads to the error bars in figure 21. We approximated the positions of the nSDBDs in the reference by hand and set an estimated ϕ value between 45–70° and 0° for equation (16). In figure 21

the triangular points are the mean value between maximum and minimum. Taking into account the fact that $\phi = 0^\circ$ is only possible on the leading edge, the exact positions of the triangular points should be lower than the current positions.

Two lines are drawn using $y = \eta x$ in figure 21, with corresponding η values marked. The points above the red lines refer to failed cases while the points below the green ones refer to successful cases. We conclude that the heating efficiency η is in the range between 3.5% and 5.0%. This value is very close to $\eta_{FGH} \approx 6\%$, indicating again that FGH plays a key role in nSDBD assisted anti-icing.

5. Summaries and conclusions

The discharge and heating features of nSDBD in anti-icing configuration has been studied with a 2D model and existing experimental data. The mechanisms of nSDBD-based plasma-assisted anti-icing have been analyzed. The parallel PASSKEY code validated by experimental measurements in this work and in Chen *et al* [36] was used.

Discharges in the exposed–encapsulated–exposed electrode configurations have been studied. The evolution of the electron density and electric field in two counter-propagating surface streamers under two conditions (7kV, 800 ns long pulse and 20kV, 20 ns short pulse) were analyzed. The electric field is directed towards another electrode during voltage rise, then directed mainly towards the dielectric surface when the streamers approach each other, and finally reversed at the trailing edge. It is observed numerically that if the sum of the analytical discharge lengths of the two streamers (affected mainly by peak voltage) is significantly larger than the electrode distance, the streamers will be ‘connected’, otherwise they will slow down and stop.

For the gas, the temperature rises in one pulse and in one duty cycle were studied. There is a 30 K increase in the first 200 ns near the electrode due to FGH. Even under the assumption that all the deposited energy is converted to gas heating, the heated discharge region is not sustainable at experimental airflow velocity (65 m s^{-1}).

For the solid, the temperature rises due to ion bombardment in one pulse and heat diffusion from gas in one duty cycle were estimated. At the end of the first voltage pulse, the order of temperature rise is 10^{-3} K at several micrometers depth. Heat diffusion from the gas leads to a temperature rise 5–10 times higher than via ion bombardment. The thermal flux from the discharge region into the water/ice layer is capable of heating it above 0°C .

The impact of ‘micro-shockwaves’ and droplet vaporization could be neglected. It takes only 75–125 ns for the droplet to reduce by 5 nm (corresponding to the maximum thickness of the water film formed on the surface at the end of each duty cycle), indicating that the heat flux from the heated gas directly to the water/ice layer is the main mechanism of nSDBD-based plasma-assisted anti-icing. In such a short time scale, the energy comes mainly from FGH.

The fraction of total energy transferred to FGH $\eta_{FGH} \approx 6\%$. The fraction of total energy required for

preventing ice formation $\eta \approx 3.5\%–5.0\%$, slightly lower than η_{FGH} .

The mechanism revealed and the fractional ratio η obtained in this paper provide the basis for designing power supply and nSDBD parameters in anti-icing applications and before the costly icing wind tunnel experiments; for a certain value of LWC and known power supply parameters, a velocity–temperature line can be drawn and used in future nSDBD-based icing control systems, and can be coupled with existing on-plane detectors.

There remains some discussion on the mechanisms of acSDBD-based anti-icing, as the role of FGH in acSDBD is negligible. Analysis of acSDBD in anti-icing experiments will be presented in subsequent papers.

Acknowledgments

The work was partially supported by the National Numerical Windtunnel Project NNW2018-ZT3B08, the National Basic Research Program of China (No. 2015CB755802) and the National Natural Science Foundation of China (Nos. 51907204, 51790511, 51522606, 91941105, 91941301). The authors are thankful to the young research group in Atelier des Plasmas for fruitful discussions.

ORCID iDs

Yifei Zhu  <https://orcid.org/0000-0001-8989-0051>

Yun Wu  <https://orcid.org/0000-0002-8575-0665>

References

- [1] Roth J R, Sherman D M and Wilkinson S P 2000 Electrohydrodynamic flow control with a glow-discharge surface plasma *AIAA J.* **38** 1166–72
- [2] Roth J R 2003 Aerodynamic flow acceleration using paraelectric and peristaltic electrohydrodynamic effects of a one atmosphere uniform glow discharge plasma *Phys. Plasmas* **10** 2117–26
- [3] Enloe C, McLaughlin T E, VanDyken R D, Kachner K, Jumper E J, Corke T C, Post M and Haddad O 2004 Mechanisms and responses of a single dielectric barrier plasma actuator: geometric effects *AIAA J.* **42** 595–604
- [4] Enloe C, McHarg M and McLaughlin T E 2008 Time-correlated force production measurements of the dielectric barrier discharge plasma aerodynamic actuator *J. Appl. Phys.* **103** 073302
- [5] Takashima K, Yin Z and Adamovich I V 2012 Measurements and kinetic modeling of energy coupling in volume and surface nanosecond pulse discharges *Plasma Sources Sci. Technol.* **22** 015013
- [6] Popov N 2013 Fast gas heating initiated by pulsed nanosecond discharge in atmospheric pressure air *51st AIAA Aerospace Sciences Meeting (AIAA Reston, VA)*
- [7] Flitti A and Pancheshnyi S 2009 Gas heating in fast pulsed discharges in N₂-O₂ mixtures *Eur. Phys. J. Appl. Phys.* **45** 21001
- [8] Aleksandrov N, Kindysheva S, Nudnova M and Starikovskiy A Y 2010 Mechanism of ultra-fast heating in a non-equilibrium weakly ionized air discharge plasma in high electric fields *J. Phys. D: Appl. Phys.* **43** 255201
- [9] Opaits D, Roupasov D, Starikovskaia S, Starikovskii A Y, Zavalov I and Saddoughi S 2005 Plasma control of boundary layer using low-temperature non-equilibrium plasma of gas discharge *AIAA Paper* **1180** 2005
- [10] Starikovskii A Y, Nikipelov A, Nudnova M and Roupasov D 2009 SDBD plasma actuator with nanosecond pulse-periodic discharge *Plasma Sources Sci. Technol.* **18** 034015
- [11] Leonov S, Opaits D, Miles R and Soloviev V 2010 Time-resolved measurements of plasma-induced momentum in air and nitrogen under dielectric barrier discharge actuation *Phys. Plasmas* **17** 113505
- [12] Rethmel C, Little J, Takashima K, Sinha A, Adamovich I and Samimy M 2011 Flow separation control using nanosecond pulse driven DBD plasma actuators *Int. J. Flow Control* **3** 213–32
- [13] Bisek N J, Poggie J, Nishihara M and Adamovich I 2014 Hypersonic flow over a cylinder with a nanosecond pulse electrical discharge *J. Thermophys. Heat Transfer* **28** 18–26
- [14] Bayoda K, Benard N and Moreau E 2015 Nanosecond pulsed sliding dielectric barrier discharge plasma actuator for airflow control: electrical, optical, and mechanical characteristics *J. Appl. Phys.* **118** 063301
- [15] Rodrigues F, Pascoa J and Trancossi M 2018 Heat generation mechanisms of dbd plasma actuators *Exp. Thermal Fluid Sci.* **90** 55–65
- [16] Gent R W, Dart N P and Cansdale J T 2017 Aircraft icing *Phil. Trans. R. Soc. A* **358** 2873–911
- [17] Lynch F T and Khodadoust A 2001 Effects of ice accretions on aircraft aerodynamics *Prog. Aerosp. Sci.* **37** 669–767
- [18] Liu Y and Hu H 2018 An experimental investigation on the unsteady heat transfer process over an ice accreting airfoil surface *Int. J. Heat Mass Transfer* **122** 707–18
- [19] Van den Broecke J 2016 De-icing using ns-DBD plasma actuators *PhD Thesis* Delft University of Technology
- [20] Meng X, Cai J, Tian Y, Han X and Zhang D 2016 Experimental Study of Anti-icing and Deicing on a Cylinder by DBD plasma actuation *47th AIAA Plasmadynamics and Lasers Conf.* p 4019
- [21] Cai J, Tian Y, Meng X, Han X, Zhang D and Hu H 2017 An experimental study of icing control using DBD plasma actuator *Exp. Fluids* **58** 102
- [22] Hu H, Zhou W, Liu Y and Kolbakir C 2017 An explorative study to use DBD plasma generation for aircraft icing mitigation *APS Meeting Abstracts*
- [23] Liu Y, Kolbakir C and Hu H 2018 A comparison study on AC-DBD plasma and electrical heating for aircraft icing mitigation *AIAA Aerospace Sciences Meeting* pp 1–20
- [24] Zhou W, Liu Y, Hu H, Hu H and Meng X 2018 Utilization of thermal effect induced by plasma generation for aircraft icing mitigation *AIAA J.* **56** 1097–104
- [25] Hu H, Kolbakir C, Hu H and Liu Y 2018 Utilizing thermal effect induced by dielectric-barrier-discharge (DBD) plasma for aircraft icing mitigation *Bull. Am. Phys. Soc.* **63** 13
- [26] Kolbakir C, Liu Y, Hu H, Starikovskiy A and Miles R B 2018 An experimental investigation on the thermal effects of NS-DBD and AC-DBD plasma actuators for aircraft icing mitigation *AIAA Aerospace Sciences Meeting* pp 1–10
- [27] Liu Y, Kolbakir C, Hu H, Starikovskiy A and Miles R 2018 An experimental study on the thermal characteristics of NS-DBD plasma actuation and application for aircraft icing mitigation *Plasma Sources Sci. Technol.* **28** 014001
- [28] Liu Y, Kolbakir C, Hu H and Hu H 2018 A comparison study on the thermal effects in dbd plasma actuation and electrical heating for aircraft icing mitigation *Int. J. Heat Mass Transfer* **124** 319–30
- [29] Liu Y, Kolbakir C, Hu H and Hu H 2018 An explorative study to use thermal effects of duty-cycled plasma actuation for aircraft icing mitigation *Atmospheric and Space Environments Conf.* pp 1–16

- [30] Liu Y, Ma L, Wang W, Kota A K and Hu H 2018 An experimental study on soft PDMS materials for aircraft icing mitigation *Appl. Surf. Sci.* **447** 599–609
- [31] Liu Y, Kolbakir C and Hu H 2018 A parametric study to explore ns-DBD plasma actuation for aircraft icing mitigation *Flow Control Conf.* pp 1–20
- [32] Tian Y, Zhang Z, Cai J, Yang L and Kang L 2018 Experimental study of an anti-icing method over an airfoil based on pulsed dielectric barrier discharge plasma *Chin. J. Aeronaut.* **31** 1449–60
- [33] Kolbakir C, Hu H, Liu Y and Jischke M C 2019 A hybrid anti-/de-icing strategy by combining NS-DBD plasma actuator and superhydrophobic coating for aircraft icing mitigation *AIAA Scitech Forum 2019* pp 1–11
- [34] Meng X, Hu H, Li C, Abbasi A A, Cai J and Hu H 2019 Mechanism study of coupled aerodynamic and thermal effects using plasma actuation for anti-icing *Phys. Fluids* **31** 037103
- [35] Zhu Y, Shcherbanev S, Baron B and Starikovskaia S 2017 Nanosecond surface dielectric barrier discharge in atmospheric pressure air: I. Measurements and 2d modeling of morphology, propagation and hydrodynamic perturbations *Plasma Sources Sci. Technol.* **26** 125004
- [36] Chen J, Liang H, Wu Y, Wei B, Zhao G, Tian M and Xie L 2018 Experimental study on anti-icing performance of NS-DBD plasma actuator *Appl. Sci.* **8** 1889
- [37] Wei B, Wu Y, Liang H, Zhu Y, Chen J, Zhao G, Song H, Jia M and Xu H 2019 SDBD based plasma anti-icing: a stream-wise plasma heat knife configuration and criteria energy analysis *Int. J. Heat Mass Transfer* **138** 163–72
- [38] Jia Y, Sang W and Cai Y 2018 Anti-icing property of nsdbd plasma actuator based on numerical simulation *Acta Aeronaut. Astronaut. Sin.* **39** 121652 (in Chinese)
- [39] Zhu Y 2018 Numerical study of nanosecond capillary and surface dielectric barrier discharges: kinetics, transport and fluid responses *PhD Thesis Ecole Polytechnique*
- [40] Bourdon A, Pasko V, Liu N, Célestin S, Ségur P and Marode E 2007 Efficient models for photoionization produced by non-thermal gas discharges in air based on radiative transfer and the Helmholtz equations *Plasma Sources Sci. Technol.* **16** 656
- [41] Luque A, Ebert U, Montijn C and Hundsdoerfer W 2007 Photoionization in negative streamers: fast computations and two propagation modes *Appl. Phys. Lett.* **90** 081501
- [42] Zhelezniak M, Mnatsakanian A K and Sizykh S V 1982 Photoionization of nitrogen and oxygen mixtures by radiation from a gas discharge *High Temp. Sci.* **20** 423–8
- [43] Tetens O 1930 Über einige meteorologische begriffe *Z. Geophys.* **6** 297–309
- [44] Hagelaar G and Pitchford L 2005 Solving the boltzmann equation to obtain electron transport coefficients and rate coefficients for fluid models *Plasma Sources Sci. Technol.* **14** 722
- [45] Trinity database (www.lxcat.net/TRINITI)
- [46] Zhu Y and Starikovskaia S M 2018 Fast gas heating of nanosecond pulsed surface dielectric barrier discharge: Spatial distribution and fractional contribution from kinetics *Plasma Sources Sci. Technol.* **27** 124007
- [47] Pancheshnyi S, Nudnova M and Starikovskii A 2005 Development of a cathode-directed streamer discharge in air at different pressures: experiment and comparison with direct numerical simulation *Phys. Rev. E* **71** 016407
- [48] Popov N 2011 Fast gas heating in a nitrogen–oxygen discharge plasma: I. Kinetic mechanism *J. Phys. D: Appl. Phys.* **44** 285201
- [49] Komuro A and Ono R 2014 Two-dimensional simulation of fast gas heating in an atmospheric pressure streamer discharge and humidity effects *J. Phys. D: Appl. Phys.* **47** 155202
- [50] Phelps A and Pitchford L 1985 Anisotropic scattering of electrons by N₂ and its effect on electron transport *Phys. Rev. A* **31** 2932
- [51] Marode E, Djerroune D, Dessante P, Deniset C, Ségur P, Bastien F, Bourdon A and Laux C 2009 Physics and applications of atmospheric non-thermal air plasma with reference to environment *Plasma Phys. Control. Fusion* **51** 2136–45
- [52] Howard C J, Fehsenfeld F C and Mcfarland M 1974 Negative ion-molecule reactions with atomic hydrogen in the gas phase at 296 k *J. Chem. Phys.* **60** 5086–9
- [53] Komuro A, Ono R and Oda T 2013 Behaviour of OH radicals in an atmospheric-pressure streamer discharge studied by two-dimensional numerical *J. Phys. D: Appl. Phys.* **46** 175206
- [54] Magne L, Pasquiers S, Gadonna K, Jeanney P, Blinsimand N, Jorand F and Postel C 2009 Oh kinetic in high-pressure plasmas of atmospheric gases containing c2h6 studied by absolute measurement of the radical density in a pulsed homogeneous discharge *J. Phys. D: Appl. Phys.* **42** 165203
- [55] Kreckel H, Bruhns H, Czek M, Glover S C, Miller K A, Urbain X and Savin D W 2010 Experimental results for h2 formation from h- and h and implications for first star formation *Science* **329** 69–71
- [56] Mcewan M J and Phillips L F 1976 Chemistry of the atmosphere *Phys. Today* **29** 54–5
- [57] Atkinson R, Baulch D L, Cox R A, Crowley J N, Hampson R F, Hynes R G, Jenkin M E, Rossi M J, Troe J and Subcommittee I 2006 Evaluated kinetic and photochemical data for atmospheric chemistry: Volume ii—gas phase reactions of organic species *Atmos. Chem. Phys.* **6** 7359
- [58] Chen C, Liu D X, Liu Z C, Yang A J, Chen H L, Shama G and Kong M G 2014 A model of plasma-biofilm and plasma-tissue interactions at ambient pressure *Plasma Chem. Plasma Process.* **34** 403–41
- [59] Liu Z C, Liu D X, Chen C, Li D, Yang A J, Rong M Z, Chen H L and Kong M G 2015 Physicochemical processes in the indirect interaction between surface air plasma and deionized water *J. Phys. D: Appl. Phys.* **48** 495201
- [60] Pipa A V, Hoder T and Brandenburg R 2013 On the role of capacitance determination accuracy for the electrical characterization of pulsed driven dielectric barrier discharges *Contrib. Plasma Phys.* **53** 469–80
- [61] Soloviev V R 2019 Analytical model of a surface barrier discharge development *Plasma Phys. Rep.* **45** 264–76
- [62] Douat C, Bauville G, Fleury M, Laroussi M and Puech V 2012 Dynamics of colliding microplasma jets *Plasma Sources Sci. Technol.* **21** 034010
- [63] Jánký J and Bourdon A 2014 Simulation of two counter-propagating helium discharges at atmospheric pressure *Plasma Sources Sci. Technol.* **23** 025001
- [64] Bin Z 2012 Characteristic analysis of single waterdroplet in evaporative supercooled process *J. Southeast Univ.* **42** 664–9
- [65] Anokhin E, Kuzmenko D, Kindysheva S, Soloviev V and Aleksandrov N 2015 Ignition of hydrocarbon: air mixtures by a nanosecond surface dielectric barrier discharge *Plasma Sources Sci. Technol.* **24** 045014
- [66] Soloviev V and Krivtsov V 2015 Analytical and numerical estimation of the body force and heat sources generated by the surface dielectric barrier discharge powered by alternating voltage *6th European Conf. for Aeronautics and Space Science (EUCASS2015)* vol 29